

Fabrication of MAPbBr₃ Single Crystal p-n Photodiode and n-p-n Phototriode for Sensitive Light Detection Application

Feng-Xia Liang, Jing-Jing Jiang, Yao-Zu Zhao, Zhi-Xiang Zhang, Di Wu, Long-Hui Zeng, Yuen Hong Tsang,* and Lin-Bao Luo*

In this study, MAPbBr₃ single crystal (MSC) p-n perovskite homojunction photodiode and n-p-n phototriode are successfully fabricated through controlled incorporation of Bi³⁺ ions in solution. Optoelectronic analysis reveals that the photodiode shows typical photovoltaic behavior and the best photovoltaic performance can be achieved when the n-type MSC is grown in 0.3% Bi³⁺ feed solution. The as-assembled p-n MSC photovoltaic detector displays obvious sensitivity to 520 nm illumination, with a high responsivity of up to 0.62 A W⁻¹ and a specific detectivity of 2.16 × 10¹² Jones, which surpass many those of MSC photodetectors previously reported. Further performance optimization can be realized by constructing an n-p-n phototriode using the same growth method. The photocurrent magnification rate of the as-fabricated n-p-n phototriode can reach a maximum value of 2.9 × 10³. Meanwhile, a higher responsivity of 14.47 A W⁻¹, specific detectivity of 4.67 × 10¹³ Jones, and an external quantum efficiency of up to 3.46 × 10³ are achieved under an emitter–collector bias of 8 V. These results confirm that the present p-n and n-p-n MSC homojunctions are promising device configurations, which may find potential application in future optoelectronic devices and systems.

and superior optoelectronic characteristics,^[1–3] which have been widely employed in a number of optoelectronic devices including photodetectors,^[4–6] lasers,^[7] light emitting diodes,^[8,9] and solar cell.^[10–12] In comparison with its polycrystalline thin film counterpart, perovskite in the form of single crystals (PSCs) have the merits of various unique properties, for example, low trap-density, long diffusion length, high carrier mobility, and excellent stability.^[13,14] These fascinating characteristics have made PSCs potentially important for fabricating highly sensitive and dependable photodetectors. In this regard, more and more attention have been devoted to the investigation of PSCs growth and their related device applications. For instance, Fang et al. had presented a narrowband perovskite photodetector, which was fabricated through the evaporation of Au and Ga electrodes on the opposite side of the bulk MAPbBr₃

1. Introduction

In the past decade, perovskite materials with a typical chemical formula of ABX₃ have received worldwide research interest because of their feasible wet-chemistry synthesis process

single crystal (MSC). The as-assembled device exhibited a very narrow external quantum efficiency (EQE) peak with a full-width at half maximums <20 nm.^[15] Recently, Ding and his colleagues have also demonstrated a self-driven photodetector by assembling an asymmetric Schottky junction on MAPbI₃ single crystals and a responsivity of 0.24 A W⁻¹ without bias was achieved.^[16] What is more, a large number of studies have been carried out on PSC photodetector composed of photoconductors,^[17,18] and metal-semiconductor-metal photodetectors.^[19] In spite of these progresses, little work has been carried out to study the optoelectronic characteristics of PSC photodetector based on perovskite p-n photodiode or n-p-n phototriode, which are elementary building blocks for various optoelectronic devices applications.

Like conventional semiconductor materials, impurity doping plays a significant role in determining the electronic and optoelectronic of perovskite related devices applications, because of the convenient manipulation of both electrical and optical properties. Hitherto, various efforts have been devoted to doping the perovskite materials through incorporating isovalent and heterovalent ions (e.g., Sr²⁺, Cd²⁺, Sn²⁺, Bi³⁺, Sb³⁺, etc.) into the crystal structure.^[20–24] For instance, Abdelhady et al. have successfully doped different kinds of ions (e.g., Bi³⁺, Au³⁺, or In³⁺) into MAPbX₃ through an in situ chemical route. They found the enhancement of electrical conductivity and bandgap narrowing after Bi³⁺ doping.^[23] Moreover, Cheng et al. have

Dr. F.-X. Liang, J.-J. Jiang, Y.-Z. Zhao
School of Materials Science and Engineering and Anhui Provincial Key
Laboratory of Advanced Functional Materials and Devices
Hefei University of Technology
Hefei 230009, China

Z.-X. Zhang, Prof. L.-B. Luo
School of Electronic Science and Applied Physics
Hefei University of Technology
Hefei 230009, China
E-mail: luolb@hfut.edu.cn

Dr. D. Wu
School of Physics and Microelectronics
Zhengzhou University
Zhengzhou 450052, China

Dr. L.-H. Zeng, Prof. Y. H. Tsang
Department of Applied Physics and Materials Research Center
The Hong Kong Polytechnic University
Kowloon, Hung Hom, Hong Kong 99077, China
E-mail: yuen.tsang@polyu.edu.hk

 The ORCID identification number(s) for the author(s) of this article can be found under <https://doi.org/10.1002/adfm.202001033>.

DOI: 10.1002/adfm.202001033

reported the incorporation of $\text{Fe}^{2+}/\text{Fe}^{3+}$ into the crystal lattice of MAPbCl_3 single crystal and further studied its optoelectronic properties through constructing planar photodetectors.^[24]

Enlightened by the above work, we herein reported on the fabrication of p-n homojunction photodiode and n-p-n phototriode by a controlled impurity doping approach. Unlike conventional p-n heterojunction, the current p-n MSC homojunction has the superiority of minimal lattice mismatch, continuous band alignments, and smaller carried trap sites.^[25–27] Since MAPbBr_3 is reported to be an intrinsic p-type semiconductor,^[13] Bi^{3+} ions with different doping concentrations were simultaneously introduced into the crystal structure during the growth of MSC in feed solution, to form p-n homojunction photodiodes. The as-fabricated devices exhibit typical photovoltaic characteristics under light illumination, and the largest photocurrent was achieved when the n-type perovskite was grown in a 0.3% Bi^{3+} feed solution (wt%). Moreover, the self-driven photodiodes showed excellent optoelectronic characteristics in terms of a high responsivity (R) of up to 0.62 A W^{-1} , a specific detectivity (D^*) of 2.16×10^{12} Jones, and robust environmental stability. At last, utilizing the photocurrent magnification effect of the perovskite phototriode, we also achieved an enhanced visible light photodetector, with a gain factor (β) as high as 2.9×10^3 . Accordingly, under a bias of 8 V, the responsivity and specific detectivity of the phototriode were increased to 14.47 A W^{-1} and 4.67×10^{13} Jones, respectively. The above results suggest that the present p-n photodiode and n-p-n phototriode MSC homojunctions are ideal building blocks for assembly of sensitive photodetector.

2. Results and Discussion

Figure 1a shows the schematic illustration of perovskite p-n homojunction. In this work, the p- and n-MSC were fabricated through a simple crystallization process.^[22] The detailed synthesis process is shown in Figure S1, Supporting Information. Briefly, the n-MSC was first grown in a heated solution composed of a mixture of PbBr_2 , MABr , and BiBr_3 . Then, the as-fabricated n-MSC was put into another precursor solution without BiBr_3 to form a wrapped external layer, which exhibits a weak p-type characteristic according to previous study. Obvious color change from orange for the pristine MSC to brown for Bi-doped MSC was observed even though the Bi^{3+} concentration of feed solution was only 0.3%. The corresponding Bi^{3+} concentration of the obtained MSC is $4.76 \times 10^{15} \text{ cm}^{-3}$, according to inductively coupled plasma mass spectrometry (ICP-MS) analysis. The inset in Figure 1b shows a typical digital photograph of the as-fabricated p-n homojunction, from which a clear interface could be easily observed. On the contrary, this interface can hardly be distinguished by the corresponding element mapping shown in Figure S2, Supporting Information, because of the relatively low doping concentration than the detection limit of energy dispersive spectrometer. From the X-ray diffraction (XRD) pattern of the ground pristine and Bi^{3+} -doped MSCs in Figure S3a, Supporting Information, strong signal ascribable to family of $\{100\}$ planes of cubic perovskite can be seen. No extra peak appears in the Bi^{3+} -doped crystal, confirming that the structure of the MSC are retained after Bi^{3+} incorporation.^[23] The Raman spectra of pristine and Bi^{3+} -doped MSC

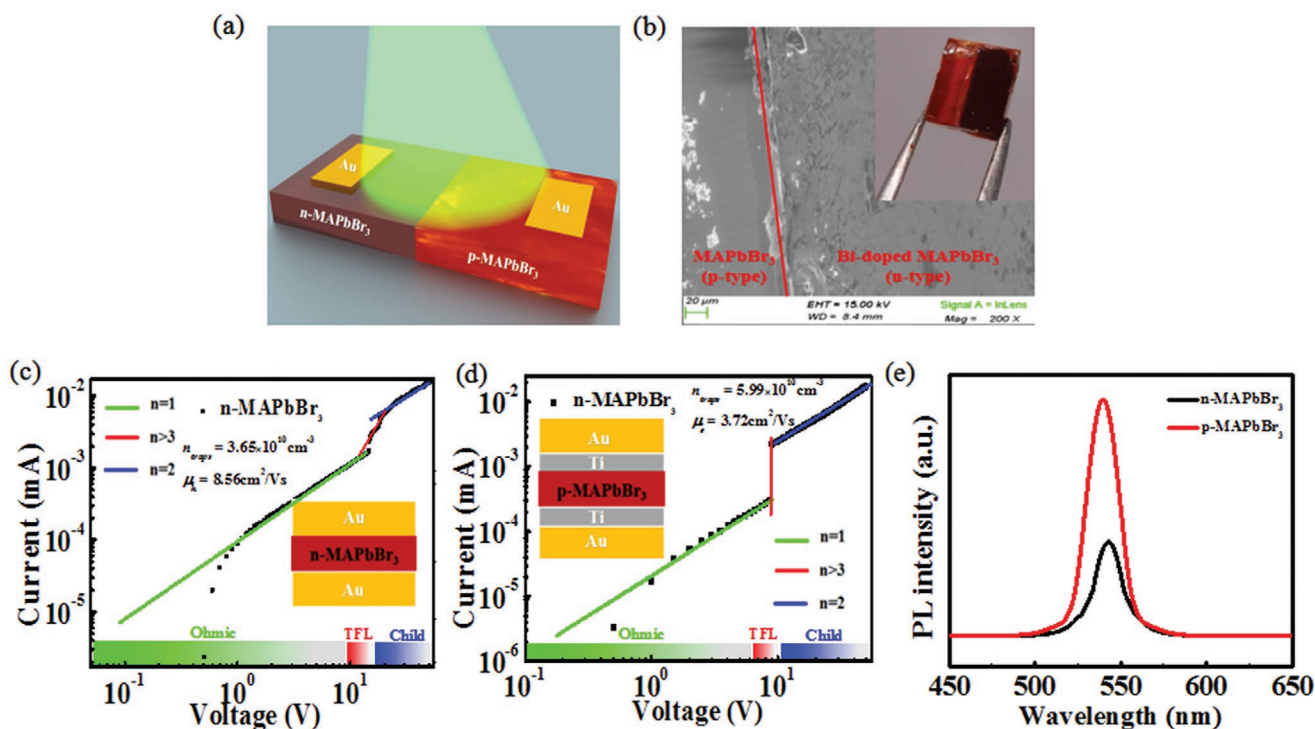


Figure 1. a) Schematic illustration of the MSC homojunction photodiode detector. b) Cross-sectional SEM image of the device, the inset shows a digital camera photograph of the MSC. c) I - V curve of a hole-only device of an n-type MSC photodetector, the inset shows the corresponding device geometry. d) I - V curve for an electron-only device of the n-type MSC photodetector, the inset shows the corresponding device geometry. e) The PL spectra of both p- and n-type MSCs.

are also compared in Figure S3b, Supporting Information. It is found that the peaks after Bi³⁺ doping are nearly identical, which means during the growth of Bi³⁺-doped perovskite, part of the Pb²⁺ site in the MSC were replaced by Bi³⁺ to form covalent bonding with bromide due to their similarity in ionic radii and the relatively high electronegativity of Bi³⁺.^[28,29] This result is actually consistent with the previous finding that the Bi–Br bond length (axial: 2.926 Å, equatorial: 2.849 Å and 2.826 Å)^[23] in the BiBr₃ is close to that of the Pb–Br bond (2.95 Å)^[13] in the octahedral structure.

To shed light on the influence of Bi³⁺ on the electrical property after impurity doping, we employed the conventional space charge limited current method to characterize the trap density and carrier mobility. For convenience, both hole-only (using Au as electrodes) and electron-only (using Ti/Au as electrodes) devices were first fabricated employing the Bi³⁺-doped MSC. Taking the hole-only Bi³⁺-doped perovskite obtained from 0.3% feed solution for example, we could clearly observe three regions in the dark *I*–*V* curve, including linear Ohmic region (green), trap-filled region (red), and trap-free Child region (blue). When operating in trap-filled region (Figure 1c), the trap-state density (*n*_{trap}) can be calculated based on the following Equations (1) and (2):^[14]

$$\epsilon = \frac{dc}{A\epsilon_0} \quad (1)$$

$$n_{\text{trap}} = \frac{2 V_{\text{TFL}} \epsilon \epsilon_0}{e d^2} \quad (2)$$

where ϵ denotes the relative dielectric constant that can be calculated by the vacuum permittivity ($\epsilon_0 = 8.85 \times 10^{-12}$ pF m⁻¹), the capacitance (*c*), the thickness of the crystal (*d*), and the surface area of the sample (*A*). The relative dielectric constant of the n-type MAPbBr₃ in this work was determined to be 3.921×10^3 based on the capacitance–frequency measurement of *c* (*c* = 21.689 pF), which is about two orders of magnitude higher than most of undoped perovskites previously reported (<100).^[30,31] The underlying reason for this abnormality is still unclear, and we speculate this high value may be due to the contribution of defects at low frequency. Moreover, by using Equation (2), the trap density (*n*_{trap}) was calculated to be 3.65×10^{10} cm⁻³, and the *V*_{TFL} can be estimated to be 8.89 V according to Figure 1c. As the voltage increases to the trap-free region, the dark current can be described by the Mott–Gurny law:^[14]

$$\mu = \frac{8 J_D d^3}{9 \epsilon \epsilon_0 V_b^2} \quad (3)$$

where *V*_b and *J*_D represent the applied voltage and dark current density, respectively. Based on the Equation (3), the hole mobility (μ_h) was estimated to be 8.56 cm² V⁻¹ s⁻¹. Similarly, the electron mobility (μ_e) and the trap density (*n*_{trap}) of the n-type MSC derived from 0.3% Bi³⁺ feed solution could be estimated through the electron-only device shown in Figure 1d. Apart from the space charge limited approach mentioned above, Hall effect analysis was also carried out to evaluate the majority carrier concentration. Table S1, Supporting

Information, summarized the main electrical transporting parameters of the MSC doped in 0.3% Bi³⁺ feed solution, pristine MSC (Figure S4, Supporting Information) studied in this work, and other reported PSCs. From these calculation results, we can easily conclude that the undoped MSC exhibits typical p-type electrical conductivity characteristic, with a hole concentration of 3.4×10^{10} cm⁻³. After Bi³⁺ doping, an electron concentration of 3.3×10^{12} cm⁻³ was obtained, which means the majority carrier has been successfully converted from holes to electrons. Moreover, the trap density for pristine MSC is about $\approx 10^9$ cm⁻³, slightly lower than many literature values.^[32–37] However, after the incorporation of Bi³⁺, the trap density increases to $\approx 10^{10}$ cm⁻³. Further steady-state photoluminescence (PL) spectrum in Figure 1e observed a large decrease in the PL spectral intensity after Bi³⁺ incorporation. This degradation in PL intensity should be ascribed to increased non-radiative recombination caused by the defects in the Bi-doped MAPbBr₃, which is in good accordance with the trap density measurement result.

Figure 2a shows the dark *I*–*V* curve of a typical MAPbBr₃ diode in which the n-type perovskite is doped with 4.76×10^{15} cm⁻³ of Bi³⁺ ion, corresponding to the 0.3% Bi³⁺ feed solution (wt%). It is obvious that the MSC diode exhibits typical rectifying behavior with a rectification ratio of about 10 at ± 3 V. As obvious good contact with negligible contact barrier were formed for both Au/p-MAPbBr₃/Au and Au/n-MAPbBr₃/Au structures (Figure S5, Supporting Information), the above rectifying characteristic which has also been observed in other controlled homojunction devices with various doping levels can be exclusively ascribed to the p-n interface.^[22] Notably, when the device was irradiated by 520 nm light, one can observe apparent photovoltaic characteristic (Figure 2b). This photovoltaic performance is relatively poor in comparison with other perovskite solar cell, however, it can enable the present device to detect optical signal without external power supply. The capability of the p-n homojunction photodiodes for light detection was then evaluated by fabricating a series of p-n devices with different Bi³⁺ doping levels (The Bi³⁺ concentration is determined to be 1.44×10^{14} , 3.45×10^{14} , 1.56×10^{15} , 4.76×10^{15} , 1.03×10^{16} , 3.46×10^{16} , and 7.50×10^{16} cm⁻³ for the doped MSCs obtained from feed solution with Bi³⁺ concentration of 0.01%, 0.05%, 0.1%, 0.3%, 0.5%, 1%, and 2%, respectively). Figure 2c summarizes the *I*–*V* curves in log coordinates of different devices under the illumination of 520 nm light. It is clear that with the increase in doping level, the photovoltaic performance will slightly increase and reach the highest value when the Bi³⁺ ion concentration of the feed solution is equal to 0.3%. The corresponding photoresponse of the different devices are shown in Figure 2d, from which the photocurrent is found to increase at first and then start to drop as the Bi³⁺ concentration further increases. A maximum photocurrent of about -0.58 μ A is achieved at a light intensity of 0.42 mW cm⁻². Furthermore, the photoresponse measurement under other different light intensities were also analyzed (Figure 2e,f), confirming the same tendency as that depicted in Figure 2d. The above enhancement in photovoltaic performance is reasonable and could be explained as follows: the power conversion efficiency is determined by such factors as bandgap, optical absorption coefficient, exciton binding energy, carrier lifetime, carrier mobility, and so on.

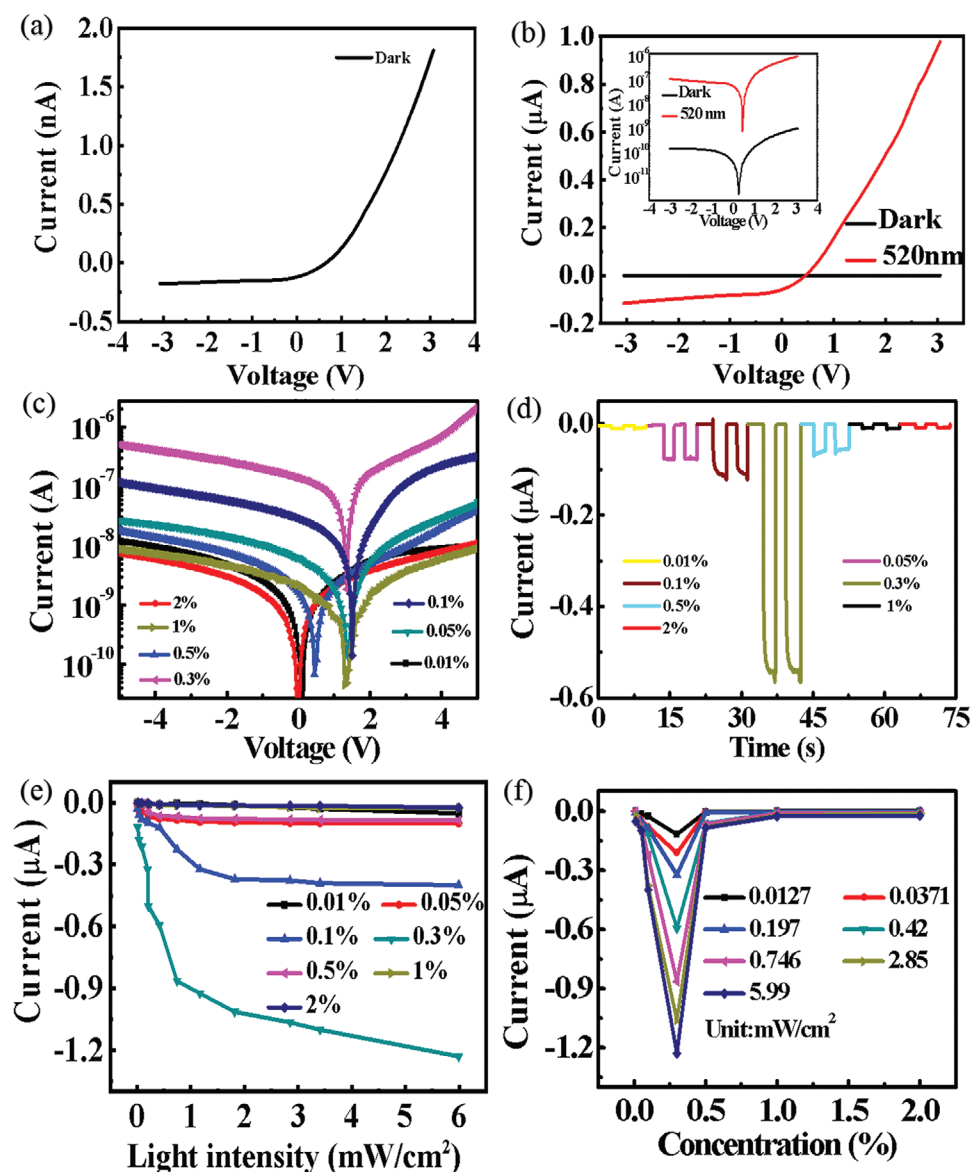


Figure 2. a) I - V curves of the MSC homojunction in darkness. b) I - V characteristics of the device in the dark and illuminated with 520 nm light ($0.0127 \text{ mW cm}^{-2}$), the inset shows I - V curves of the device in the semi-logarithmic scale. c) I - V characteristics of MSC homojunction grown in feed solution with different concentrations of Bi^{3+} : 0.01%, 0.05%, 0.1%, 0.3%, 0.5%, 1%, and 2%, under 520 nm illumination. d) Photoresponse of the homojunction photodiode device under 520 nm light (0.42 mW cm^{-2}) with different BiBr_3 concentrations at zero bias. e) Photocurrent of the homojunction device with different BiBr_3 concentrations as a function of the incident light intensity under 520 nm light at zero bias. f) Photocurrent of the devices with seven light intensities as a function of different BiBr_3 concentrations at zero bias.

For the present MSC photodiode, the doping level is usually positively correlated with the built-in potential and negatively correlated with the depletion region width (detailed influence of Bi^{3+} ions concentration on both built-in potential and depletion region width is provided in Supporting Information).^[38] Even though the Bi^{3+} doping will inevitably cause narrowing in depletion region width and decrease in both carrier mobility and carrier lifetime, which are bad for power conversion efficiency. However, in the meanwhile, modest concentration of Bi^{3+} doping can reduce the bandgap, allowing the device to harvest more photons for power conversion. On the other hand, the enhancement in built-in potential at modest doping level will

lead to more efficient separation of electron-hole pairs, which is also beneficial for high photovoltaic performance.

In light of the fact that the photodiode device assembled of n-type MSC with a medium Bi^{3+} doping concentration of $4.76 \times 10^{15} \text{ cm}^{-3}$ displays the best photoelectric characteristics, the following photoelectric performance analysis was carried out by choosing only this prototype device. **Figure 3a** shows the time-dependent photoresponse under periodically switched 520 nm light. Obviously, the perovskite photodiode can be repeatedly switched between on/off states with excellent repeatability and stability. Furthermore, the photoresponse can keep nearly unchanged after 350 cycles of illumination and even after

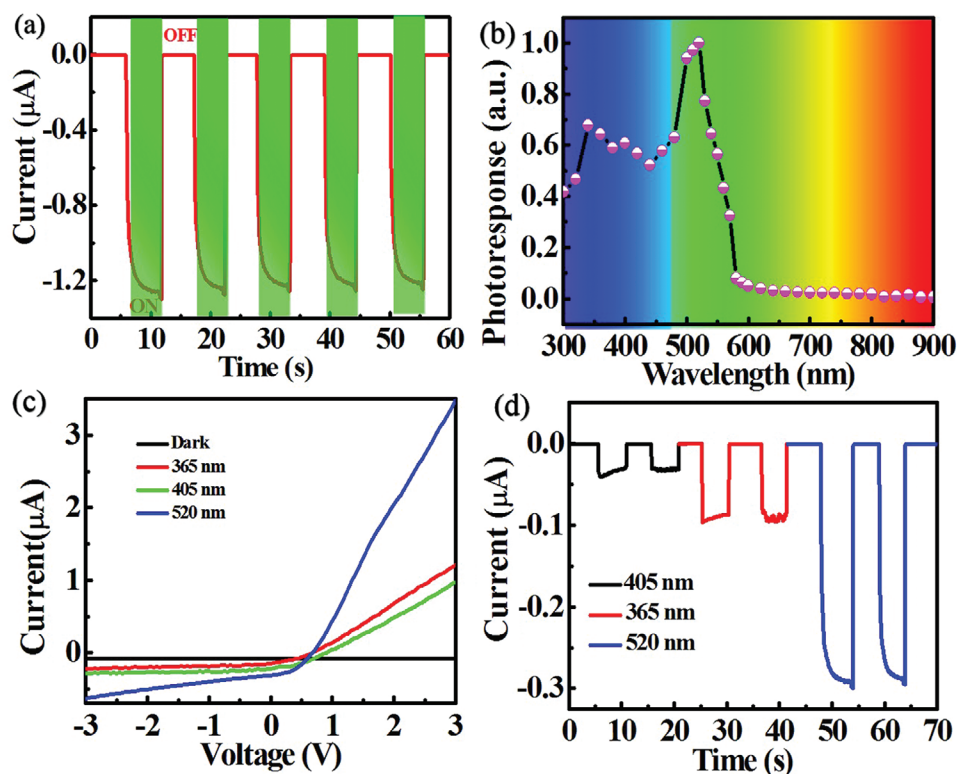


Figure 3. a) Photoresponse of photodiode composed of the n-type Bi^{3+} doped MSC with doping level of $4.76 \times 10^{15} \text{ cm}^{-3}$ under 520 nm light illumination (5.99 mW cm^{-2}) at zero bias. b) The spectral response of the perovskite photodetector. c,d) I - V curves of the device shined with various wavelengths, the power intensities are all set to be 0.197 mW cm^{-2} and photoresponse curves of the device illuminated by various wavelengths at zero bias.

45 days storage in ambient condition (Figure S6, Supporting Information). The spectral photoresponse at 0 V was further tested under a fixed light illumination with varied wavelength. As plotted in Figure 3b, the device exhibits apparent photosensitivity to light illumination from 300 to 560 nm, with the peak sensitivity located at 520 nm (Figure 3c,d).^[39] The sensitivity peak at 520 nm can be readily ascribed to the bandgap of MAPbBr_3 . While the rest two peaks at both 365 and 405 nm are associated with the incorporation of Bi^{3+} ions, which can cause luminescence band mainly in the UV region and thereby contribute to enhancement in photoresponse.^[40,41]

To further quantify the optoelectronic property of the self-powered perovskite p-n photodiode, a series of photoresponse measurement under 520 nm illumination with different light intensities at 0 V were also performed. Figure 4a,b plots the I - V curves and photoresponse of the MSC photodiodes under light intensity ranging from 0.0127 to 5.99 mW cm^{-2} . Obviously, the photocurrent has a positive correlation with the light intensity, which can be attributed to the increased population of photoexcited charge carriers under higher intensity. To reveal the dependent relationship between the photocurrent and the light intensity, the evolution of photocurrent (I) as a function of light intensity (P) can be described by the following power law:^[42]

$$I_{\text{ph}} \propto P^\theta \quad (4)$$

where θ is determined by the linear relationship of light intensity and photocurrent. Through fitting the curves at

two different regions (weak light intensity from 0.0127 to 0.76 mW cm^{-2} and high light intensity from 0.76 to 5.99 mW cm^{-2}), two different θ values of 0.53 and 0.18 are obtained, respectively. These two exponents that deviate from the ideal value ($\theta = 1$) indicate the loss of photogenerated carriers due to strong recombination activity during the photodetection process. Furthermore, the relatively lower value of θ at higher light intensity is reasonable as the recombination loss in the perovskite or at the junction interface will become more serious than that at low light intensity.^[43,44] Similar tendency was also observed on photovoltage and on/off ratio. As shown in Figure 4d,e, both photovoltage and on/off ratio are found to increase with increasing light intensity. Specifically, the on/off ratio can achieve a maximum value of 2.68×10^3 when the light intensity is as high as 5.99 mW cm^{-2} . For quantitative description of the MSC photodiode device, the key-figure-of-merit parameters of the responsivity (R) and specific detectivity (D^*) were calculated. The R indicates the photocurrent generated per unit power of the incident light on the effective area of a photodetector, which can be expressed as:^[42]

$$R = \frac{I_\lambda - I_d}{P_\lambda S} \quad (5)$$

where I_λ is the photocurrent, I_d is the dark current ($I_d = -4.8 \times 10^{-10} \text{ A}$), P_λ is the incident 520 nm intensity, and S is the effective illuminated area ($S = 0.015 \text{ cm}^2$). The specific detectivity (D^*) represents the ability of a photodetector to probe weak

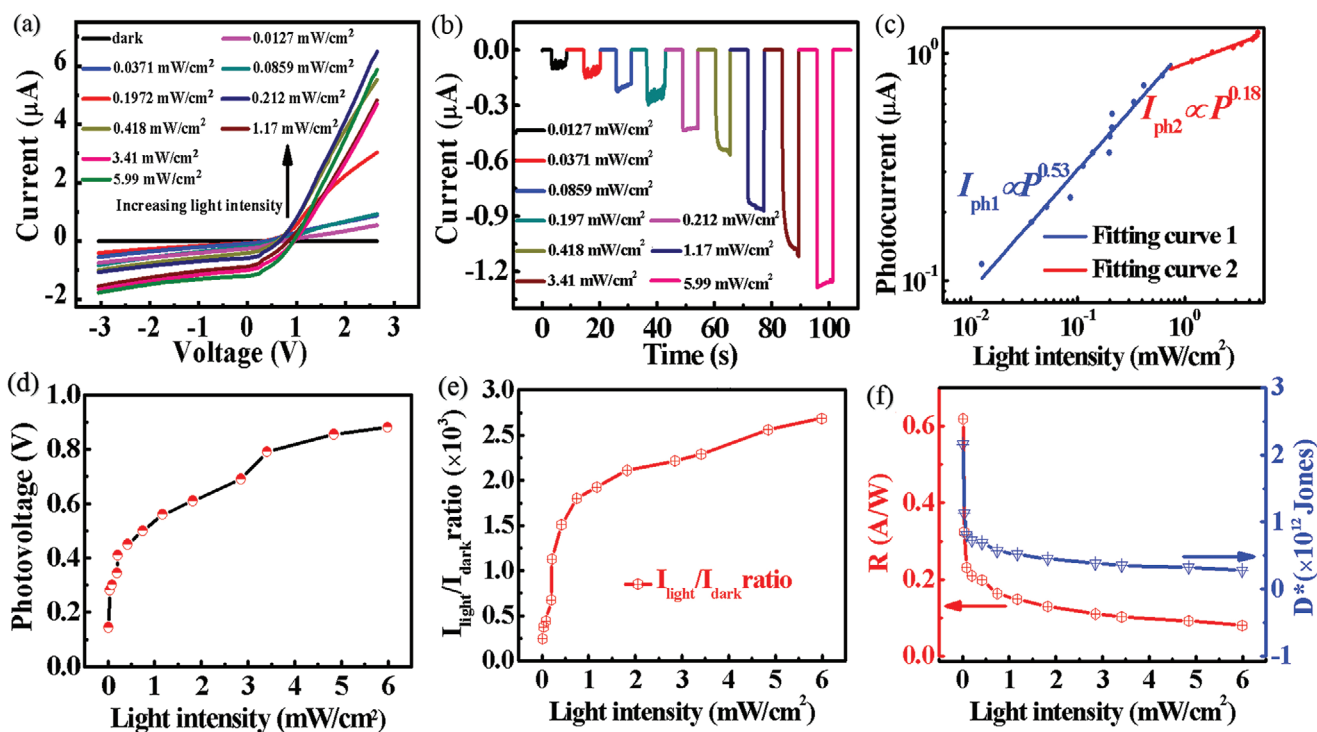


Figure 4. a) I - V curves of the homojunction device under 520 nm light with various light intensities. b) Photoresponse of the homojunction device under 520 nm light with different light intensities at zero bias. c) The photocurrent at zero bias voltage as a function of light intensity. d) The photovoltage of the different light intensity at zero bias. e) $I_{\text{light}}/I_{\text{dark}}$ ratio as a function of the incident light intensity. f) The responsivity and specific detectivity as a function of the incident light intensity under 520 nm light.

optical signal and can be described by noise equivalent power (NEP) from the following expressions:^[45]

$$D^* = \frac{\sqrt{S\Delta f}}{NEP} \quad (6)$$

$$NEP = \frac{\sqrt{i_n^2}}{R} \quad (7)$$

where Δf is the specific bandwidth, and $\sqrt{i_n^2}$ is the root mean square value of the noise current. According to the spectral density of the photodiode at different frequencies in Figure S7b, Supporting Information, the noise level of $\sqrt{i_n^2}$ was acquired to be 3.5×10^{-14} A Hz^{-1/2} at the bandwidth of 1 Hz. Based on these constants and equations, both R and D^* under different light intensities were calculated and displayed in Figure 4f. We notice that both R and D^* values will decrease with increasing light intensity. Specifically, as the illumination intensity is as weak as 0.0127 mW cm⁻², both metrics can reach the maximum values of 0.62 A W⁻¹ and 2.16×10^{12} Jones, respectively. **Table 1** compares the main parameters of the present p-n homojunction photodiodes and other self-powered perovskite-based devices. Apparently, both R and D^* are comparable to some well-studied polycrystalline film photodetectors with solar cell like structure,^[46-48] but are much better than the devices composed of PSCs crystal based Schottky junction^[16,49] and heterojunction photodetectors.^[50]

To shed light on the operation mechanism of the present self-driven homojunction photodiode, the energy band diagram of the photodiode was then analyzed. **Figure 5a,b** shows the ultraviolet photoelectron spectra (UPS) of the Bi³⁺-doped MSC for determining the energy band position of the n-MSC. The valance band maximum (E_{VBM}) of the n-MSC was estimated to be -6.13 eV, according to the method reported previously.^[51] The absorption edge slightly shifts from 560 nm for p-MSC to 580 nm for n-MSC as depicted in Figure 5c. Based on the absorption curves, we could further determine the change of bandgap by using the Kubelka-Munk equation:^[52] $(\alpha h\nu)^2 = A(h\nu - E_g)$, where α and $h\nu$ represent the absorption coefficient and incident photo energy, respectively. The inset of Figure 5c shows the Tauc plot of the absorption spectrum for both n-type and p-type MSCs, whose bandgap was estimated to be 2.12 and 2.17 eV, respectively. Such a slight narrowing in bandgap after Bi³⁺ doping is consistent with other doped MSC which has been reported previously.^[23] What is more, the conduction band minimum (E_{CBM}) of the n-MSC was calculated to be -4.01 eV. On the basis of these parameters, the energy band diagram of p-n homojunction photodiode is depicted in Figure 5d, which obviously exhibits a typical type II homojunction. The working mechanism of this self-driven photodetector can be explained as follows: once p-type and n-type MSCs are in contact with each other, a built-in electric field could be formed at the interface due to band bending. The direction of this electric field is pointing from n-type MSC to p-type MSC. Under the illumination of visible light, the photogenerated electron and holes in the depletion region will be separated, with the electrons drifted

Table 1. Summary of the performance of the present and other perovskite-based photodetectors.

Materials	λ [nm]	R [$A W^{-1}$]	D^* [Jones]	Bias [V]	Crystal structure	Reference
TiO ₂ /MAPbI ₃ /Spiro-OMe TAD photodiode	600	0.4	$\approx 10^{12}$	0	Polycrystal	[46]
PEDOT:PSS/PbS QDs/MAPbI ₃ /PC ₆₁ BM photodiode	900	0.13	5.1×10^{12}	0	Polycrystal	[47]
TiO ₂ /MAPbI ₃ /Spiro-OMe TAD photodiode	500	0.35	—	0	Polycrystal	[48]
MAPbBr ₃ Schottky junction	White light	0.002	1.4×10^{10}	0	Monocrystal	[49]
MAPbBr ₃ /MAPbBr _{3-x} graded heterojunction	455	0.27	—	0	Monocrystal	[50]
MAPbI ₃ Schottky junction	808	0.24	—	0	Monocrystal	[16]
MAPbBr ₃ single crystal homojunction	520	0.62	2.16×10^{12}	0	Monocrystal	Our work
MAPbBr ₃ single crystal phototriode	520	14.47	4.67×10^{13}	8	Monocrystal	Our work

to the n-MAPbBr₃ while the holes to the p-MAPbBr₃, forming photocurrent or photovoltage in the external circuit.

Although p-n perovskite photodiode displays apparent photoresponse to incident visible light, there is an undeniable fact that it suffers from relatively low responsivity (less than $1 A W^{-1}$) for no gain during the photodetection process. By using the same growth method, we then assembled a phototriode with a simple n⁺-p-n homojunction architecture, in which the photocurrent generated in one p-n region could be further magnified by another highly doped n⁺-p junction.^[53] Similar to conventional phototriode, the as-fabricated

n⁺-p-n homojunction is also characterized by three regions, the emitter (E, n⁺ region), the base (B, p region), and the collector (C, n region), as shown in Figure 6a. Figure 6b displays a representative SEM image of perovskite phototriode, in which clear interfaces of the emitter (0.5% Bi³⁺-doped MSC), base (pristine MSC), and collector (MSC doped in 0.3% feed solution) can be easily observed. The magnification mechanism of the perovskite phototriode can be explained by the energy band diagram in Figure 6c. The phototriode usually works with the collector reverse biased and emitter forward biased. As the light is illuminated on base-collector region, the photogenerated

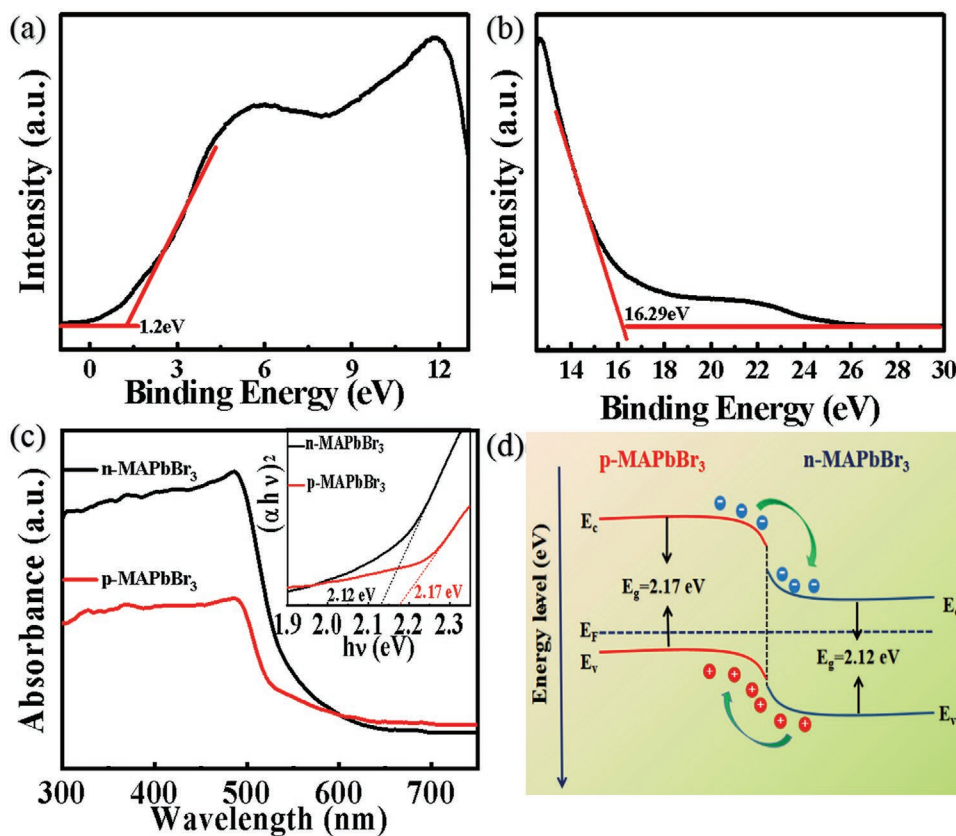


Figure 5. a) The energy difference between the Fermi level (E_F) and E_V . b) The UPS spectra of the n-MAPbBr₃ at the secondary electron cut-off edge. c) The optical absorption spectrum p- and n-MSC, the inset shows the plot of $(\alpha h\nu)^2$ versus photon energy ($h\nu$). d) Energy band diagram of MSC homojunction photodiode.

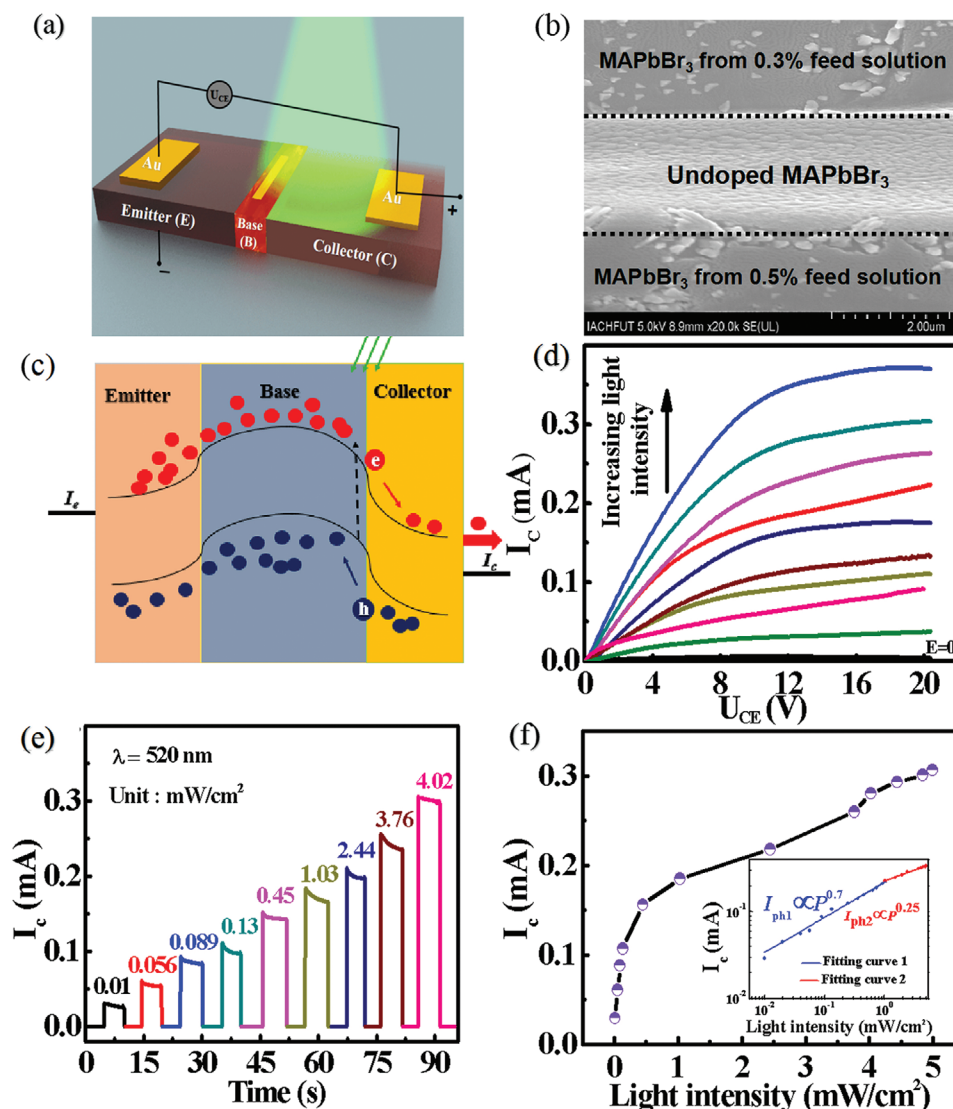


Figure 6. a) Schematic illustration of the MSC n-p-n phototriode device. b) Cross-sectional SEM image of the device. c) The equivalent circuit illustration of the working principle of an n-p-n phototriode. d) I - V curves of the phototriode device with various light intensities under 520 nm light. e) Photoresponse of the phototriode device under 520 nm light with different light intensities at 8 V bias. f) The photocurrent at 8 V bias voltage as a function of light intensity. (Inset) The curve can be fitted according to power law.

electron-hole pairs within the B-C junction are separated with electrons drifting to the n-type collector while holes drifting to the p-type base, giving rise to the photocurrent I_p as that in the photodiode. Then the holes in the base continue to diffuse across the E-B junction, which will accordingly change the bias of the E-B junction and thus induce a significant drift of electrons from highly doped n-type emitter to the base region. It should be noted that in this study, the width of the base is intentionally designed to be narrow (300 μm) so that only a relatively small part of the injected electrons recombine with the hole. The rest of electrons will however flow through the base, reach the reverse biased B-C junction, and finally be collected by the collector terminal. The collector current I_c is then amplified from the initial photocurrent I_p and the relationship between them are expressed by equations:^[25] $I_c = (1 + \beta) I_p$, where I_c is the collector current, β is the magnification rate

(or gain factor), and I_p is approximately equal to the based current that could be measured by experiment. Figure 6d shows the I_c - U_{ce} curves of the as-assembled n⁺-p-n MSC phototriode under 520 nm laser illumination with varied intensity ranging from 0.01 to 4.89 mW cm^{-2} . With the increase of the collector-emitter voltage, the photocurrent increases rapidly first and then reaches a plateau, showing the typical feature of the phototriode. In addition, through further fitting the curves of photocurrent versus light intensity, two exponents of 0.7 and 0.25 were obtained, respectively (Figure 6f).

Unlike the p-n MSC photodiode with no gain, the n⁺-p-n phototriode shows a high internal gain, which means the EQE is larger than 100%. Figure 7a exhibits the light intensity dependent gain factor, from which the gain declines with the increase of the light intensity. Specifically, a prominent gain factor of 2.9×10^3 was achieved at a weak light intensity of

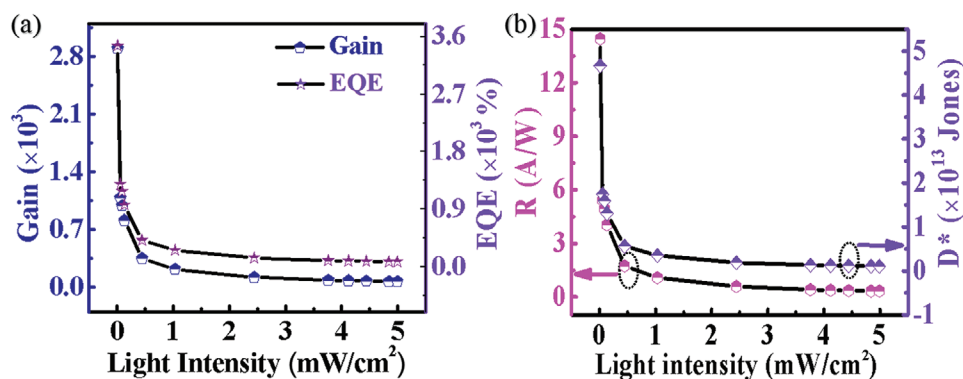


Figure 7. a) The dependence of gain and EQE of the as-fabricated MSC phototriode versus the incident light intensity at 8 V bias. b) The responsivity and specific detectivity of the device as a function of the incident light intensity at 8 V bias.

0.01 mW cm⁻². The EQE can be determined by the equation:^[54] $EQE = \frac{hcR}{e\lambda}$, where h is Planck constant, c , e , and λ represent the speed of light, the elementary electrical charge, and the incident light wavelength, respectively. The EQE under weak light also reaches a high value of 3.46×10^3 , which means that internal gain plays a significant role in the phototriode. By using Equations (5) and (6), both R and D^* at various light intensities were calculated and plotted in Figure 7b. At a relatively low light intensity, a maximum responsivity of 14.47 A W^{-1} and specific detectivity of 4.67×10^{13} Jones are obtained. Without question, these two values are much larger than that of p-n MSC homo-junction photodiode.

3. Conclusions

In summary, we have reported on the successful fabrication of a self-driven MSC p-n photodiode via doping of Bi³⁺ in the pristine MAPbBr₃ bulk single crystals. The as-fabricated MSC photodiode exhibits obvious photovoltaic effects and has the largest photocurrent as the Bi³⁺ concentration is 0.3%. A peak responsivity of up to 0.62 A W^{-1} and a specific detectivity of 2.16×10^{12} ($0.0127 \text{ mW cm}^{-2}$) were achieved under zero bias. Most importantly, this self-driven photodiode displays excellent stability, and the photocurrent remains almost constant after 45 days' storage at room temperature without any protection. Further increase in photocurrent could be realized by constructing an n-p-n MSC phototriode using the same solution approach. The magnification rate of the photocurrent can reach 2.9×10^3 , which correspondingly enhanced the responsivity (14.47 A W^{-1}) and specific detectivity (4.67×10^{13} Jones). The above results confirm that the present self-powered MSC-based photodetector may find promising applications in future optoelectronic devices.

4. Experimental Section

Materials Preparation and Device Fabrication: The methylammonium bromide (CH₃NH₂Br, ≥99.5%), lead bromide (PbBr₂, ≥98%) were purchased from Xi'an Polymer Light Technology Co. Ltd. BiBr₃ (bromide, 99%) and *N,N*-dimethylformamide (DMF) (anhydrous, ≥99.9%) were obtained from Sigma-Aldrich. The pristine MAPbBr₃ single crystal

could be grown by dissolving methylamine bromide (MABr) and PbBr₂ in a 1:1 molar ratio in 2 mL DMF, according to the previous study.^[22] Such a single crystal method could be used to synthesize the Bi³⁺-doped MAPbBr₃ single crystal as well. For the synthesis of p-n wrapped MAPbBr₃, the n-type MAPbBr₃ single crystals were first grown at 80 °C for 4 h. Then, the obtained n-type samples were put into the precursor solution without BiBr₃, with the temperature kept at 80 °C for another 4 h. Finally, the core-shell wrapped MAPbBr₃ single crystals were obtained. During the growth of n-MAPbBr₃, different content of BiBr₃ were added into the above precursor solution. To construct the p-n junction photodiode, the structure was cut so as to expose the inner n-type MAPbBr₃. The planar-type photodetector was fabricated by depositing two Au (50 nm) electrodes on the p- and n-MAPbBr₃ via electron-beam evaporation. For the fabrication of n-p-n perovskite phototriode, another external layer of n-type perovskite was further grown on p-n wrapped structure, followed by deposition of three Au (50 nm) electrodes on the emitter, base, and collector regions through the electron-beam evaporation.

Structural Analysis and Device Characterization: The morphology of perovskite single crystal was characterized by a field-emission SEM (Hitachi, SU8020). Optical absorption of pristine MAPbBr₃ and the doped MAPbBr₃ was studied with a UV-vis spectrophotometer (UV-2550, Shimadzu, Japan). The UPS analysis was performed on a VG ESCALAB 220i-XL ultrahigh vacuum surface analysis system with a base vacuum of 10⁻¹⁰ Torr equipped with a monochromatic Al K α X-ray (1486.6 eV) source. The Bi³⁺ ion concentration was determined by ICP-MS (Thermo, Neptune Plus). The capacitance of MSC device was characterized by a capacitance meter (Yangzi, YD2616). The Raman spectrum of pristine MAPbBr₃ and the Bi³⁺ doped-MAPbBr₃ were recorded on a HR Evolution (Horiba Jobin Yvon) Raman spectrometer with a 532 nm laser. The PL spectrum of the PSCs was characterized by fluorescence spectrophotometer equipped with an Xe Lamp. The crystal structures of PSCs were analyzed by XRD (Rigaku D/max-rB). The electrical measurement was performed on a semiconductor characterization system (Keithley 2400). Laser diodes with wavelengths of 365 nm (Thorlabs M365LP1), 405 nm (HA34051500-AL), and 520 nm (FU515AD30-BD10) were used as the illumination sources. The power intensity of all light sources was accurately calibrated by a power meter (Thorlabs GmbH., PM 100D). In order to achieve the spectral selectivity analysis, the monochromatic light was prepared by an Xe lamp (CEL-HXF 300) attached with a monochromator (Zolix Instruments, Omni-nx I). The optoelectronic property of PSCs phototriodes was measured by a Keithley 4200 semiconductor analyzer at room temperature.

Supporting Information

Supporting Information is available from the Wiley Online Library or from the author.

Acknowledgements

This work was supported by the National Natural Science Foundation of China (NSFC, Nos. 61575059, 61675062, 21501038), the Fundamental Research Funds for the Central Universities (JZ2018HGFB0275 and PA2020GDKC0014), Research Grants Council of Hong Kong, China (Project No. GRF 152093/18E PolyU B-Q65N), and the Open Foundation of Anhui Provincial Key Laboratory of Advanced Functional Materials and Devices (4500-411104/011).

Conflict of Interest

The authors declare no conflict of interest.

Keywords

optoelectronic devices, perovskite homojunctions, photodiodes, phototriodes, single crystals

Received: February 3, 2020

Revised: March 26, 2020

Published online: June 25, 2020

- [1] J. Burschka, N. Pellet, S. Moon, R. Humphry-Baker, P. Gao, M. K. Nazeeruddin, M. Grätzel, *Nature* **2013**, 499, 316.
- [2] F. X. Liang, J. Z. Wang, Z. X. Zhang, Y. Y. Wang, Y. Gao, L. B. Luo, *Adv. Opt. Mater.* **2017**, 5, 1700654.
- [3] Z. G. Xiao, C. Bi, Y. C. Shao, Q. F. Dong, Q. Wang, Y. B. Yuan, C. G. Wang, Y. L. Gao, J. Huang, *Energy Environ. Sci.* **2014**, 7, 2619.
- [4] R. Dong, Y. J. Fang, J. Chae, J. Dai, Z. G. Xiao, Q. F. Dong, Y. B. Yuan, A. Centrone, X. C. Zeng, J. S. Huang, *Adv. Mater.* **2015**, 27, 1912.
- [5] L. T. Dou, Y. Yang, J. B. You, Z. R. Hong, W. H. Chang, G. L. Li, Y. Yang, *Nat. Commun.* **2014**, 5, 5404.
- [6] X. W. Tong, W. Y. Kong, Y. Y. Wang, J. M. Zhu, L. B. Luo, Z. H. Wang, *ACS Appl. Mater. Interfaces* **2017**, 9, 18977.
- [7] G. C. Xing, N. Mathews, S. S. Lim, N. Yantara, X. F. Liu, D. Sabba, M. Grätzel, S. Mhaisalkar, T. C. Sum, *Nat. Mater.* **2014**, 13, 476.
- [8] M. J. Yuan, L. N. Quan, R. Comin, G. Walters, R. Sabatini, O. Voznyy, Z. Lu, D. H. Kim, E. H. Sargent, *Nat. Nanotechnol.* **2016**, 11, 872.
- [9] Z. G. Xiao, R. A. Kerner, L. F. Zhao, N. L. Tran, K. M. Lee, T. W. Koh, G. D. Scholes, B. P. Rand, *Nat. Photonics* **2017**, 11, 108.
- [10] K. P. Marshall, M. Walker, R. I. Walton, R. A. Hatton, *Nat. Energy* **2016**, 1, 16178.
- [11] H. L. Hsu, C. C. Chang, C. P. Chen, B. H. Jiang, R. J. Jeng, C. H. Cheng, *J. Mater. Chem. A* **2015**, 3, 9271.
- [12] J. Beilsten-Edmands, G. E. Eperon, R. D. Johnson, H. J. Snaith, P. G. Radaelli, *Appl. Phys. Lett.* **2015**, 106, 173502.
- [13] D. Shi, V. Adinolfi, R. Comin, M. J. Yuan, E. Alarousu, A. Buin, Y. Chen, X. Zhang, Y. Losovsky, *Science* **2015**, 347, 519.
- [14] Z. Yang, Q. Xu, X. D. Wang, J. F. Lu, H. Wang, F. T. Li, L. Zhang, G. F. Hu, C. F. Pan, *Adv. Mater.* **2018**, 30, 1802110.
- [15] Y. J. Fang, Q. F. Dong, Y. C. Shao, Y. B. Yuan, J. S. Huang, *Nat. Photonics* **2015**, 9, 679.
- [16] J. Ding, H. J. Fang, Z. P. Lian, J. W. Li, Q. R. Lv, L. D. Wang, J. L. Sun, Q. F. Yan, *CrystEngComm* **2016**, 18, 4405.
- [17] F. Wang, J. J. Mei, Y. P. Wang, L. G. Zhang, H. F. Zhao, D. X. Zhao, *ACS Appl. Mater. Interfaces* **2016**, 8, 2840.
- [18] H. Deng, X. K. Yang, D. D. Dong, B. Li, D. Yang, S. J. Yuan, K. K. Qiao, Y. B. Cheng, J. Tang, H. S. Song, *Nano Lett.* **2015**, 15, 7963.
- [19] J. Yang, T. Yu, K. Zhu, Q. Y. Xu, *J. Phys. D: Appl. Phys.* **2017**, 50, 495102.
- [20] M. T. Klug, A. Osherov, A. A. Haghhighrad, S. D. Stranks, P. R. Brown, S. Bai, X. G. Dang, A. M. Belcher, *Energy Environ. Sci.* **2017**, 10, 236.
- [21] C. F. J. Lau, M. Zhang, X. F. Deng, J. H. Zheng, J. M. Bing, Q. S. Ma, S. J. Huang, A. Ho-Baillie, *ACS Energy Lett.* **2017**, 2, 2319.
- [22] X. Wang, Y. Wu, G. W. Li, J. Wu, X. B. Zhang, Q. Li, B. P. Wang, J. Chen, W. Lei, *Adv. Electron. Mater.* **2018**, 4, 1800237.
- [23] A. L. Abdelhady, M. I. Saidaminov, B. Murali, V. Adinolfi, O. Voznyy, K. Katsiev, E. H. Sargent, *J. Phys. Chem. Lett.* **2016**, 7, 295.
- [24] X. H. Cheng, L. Jing, Y. Yuan, S. J. Du, J. Zhang, X. Y. Zhan, J. X. Ding, H. Yu, G. D. Shi, *J. Mater. Chem. C* **2019**, 123, 1669.
- [25] D. A. Neamen, *Semiconductor Physics and Devices*, Vol. 3, McGraw-Hill, New York **1997**.
- [26] J. M. Shah, Y. L. Li, T. Gessmann, E. F. Schubert, *J. Appl. Phys.* **2003**, 94, 2627.
- [27] Y. Jin, D. H. Keum, S. J. An, J. Kim, H. S. Lee, Y. H. Lee, *Adv. Mater.* **2015**, 27, 5534.
- [28] B. B. Luo, F. Li, K. Xu, Y. Guo, Y. Liu, Z. G. Xia, J. Z. Zhang, *J. Mater. Chem. C* **2019**, 7, 2781.
- [29] Y. Zhou, J. Chen, O. M. Bark, H.-T. Sun, *Chem. Mater.* **2018**, 30, 6589.
- [30] Q. F. Dong, Y. J. Fang, Y. C. Shao, P. Mulligan, J. Qiu, L. Cao, J. S. Huang, *Research* **2015**, 347, 6225.
- [31] J. Z. Song, Q. Z. Cui, J. H. Li, J. Y. Xu, Y. Wang, L. M. Xu, J. Xue, Y. H. Dong, T. Tian, H. D. Sun, H. B. Zeng, *Adv. Opt. Mater.* **2017**, 5, 1700157.
- [32] H. S. Rao, W. G. Li, B. X. Chen, D. B. Kuang, C. Y. Su, *Adv. Mater.* **2017**, 29, 1602639.
- [33] Y. X. Chen, Q. Q. Ge, Y. Shi, J. Liu, D. J. Xue, J. Y. Ma, J. Ding, H. J. Yan, J. S. Hu, L. J. Wan, *J. Am. Chem. Soc.* **2016**, 138, 16196.
- [34] Z. Q. Yang, Y. H. Deng, X. W. Zhang, S. Wang, H. Z. Chen, S. Yang, R. M. Ma, *Adv. Mater.* **2018**, 30, 1704333.
- [35] Y. C. Liu, Z. Yang, D. Cui, X. D. Ren, J. K. Sun, X. J. Liu, J. R. Zhang, Q. B. Wei, H. B. Fan, F. Y. Yu, X. Zhang, C. M. Zhao, S. Z. Liu, *Adv. Mater.* **2015**, 27, 5176.
- [36] A. A. Zhumekenov, M.-I. Saidaminov, M. A. Haque, E. Alarousu, S. P. Sarmah, B. Murali, O.-F. Mohammed, *ACS Energy Lett.* **2016**, 1, 32.
- [37] Y. Yamada, M. Hoyano, R. Akashi, K. Oto, Y. Kanemitsu, *J. Phys. Chem. Lett.* **2017**, 8, 5798.
- [38] Q. D. Ou, Y. P. Zhang, Z. Y. Wang, J. A. Yuwono, R. B. Wang, Z. G. Dai, W. Li, C. G. Zheng, Z. Q. Xu, C. X. Zheng, H. Zhang, Q. L. Bao, *Adv. Mater.* **2018**, 30, 1705792.
- [39] H. Liu, X. F. Wei, Z. X. Zang, X. Y. Lei, W. C. Xu, L. B. Luo, H. L. Z, R. F. L, J. H. Liu, *J. Phys. Chem. Lett.* **2019**, 10, 786.
- [40] L. Chen, H. W. Zheng, J. G. Cheng, P. Song, G. T. Yang, G. B. Zhang, C. Wu, *J. Lumin.* **2008**, 128, 2027.
- [41] X. Y. Huang, X. H. Ji, Q. Y. Zhang, *J. Am. Ceram. Soc.* **2011**, 94, 833.
- [42] C. Y. Wu, J. W. Kang, B. Wang, H. N. Zhu, Z. J. Li, S. R. Chen, S. R. C. L. W. W. H. Y. C. X. L. B. Luo, *J. Mater. Chem. C* **2019**, 7, 11532.
- [43] C. Xie, X. T. Lu, X. W. Tong, Z. X. Zhang, F. X. Liang, L. Liang, Y. C. Wu, *Adv. Funct. Mater.* **2019**, 29, 1806006.
- [44] L. H. Zeng, M. Z. Wang, H. Hu, Y. Q. Yu, C. Y. Wu, L. Wang, J. G. Hu, C. Xie, F. X. Liang, L. B. Luo, *ACS Appl. Mater. Interfaces* **2013**, 5, 9362.
- [45] W. G. Li, X. D. Wang, J. F. Liao, Y. J. Jiang, D. B. Kuang, *Adv. Funct. Mater.* **2020**, 30, 1909701.
- [46] B. R. Sutherland, A. K. Johnston, A. H. Ip, J. Xu, V. Adinolfi, P. Kanjanaboos, E. H. Sargent, *ACS Photonics* **2015**, 2, 1117.

- [47] C. Liu, K. Wang, P. C. Du, E. M. Wang, X. Gong, A. J. Heeger, *Nanoscale* **2015**, *7*, 16460.
- [48] S. Casaluci, L. Cinà, F. Matteocci, P. Lugli, A. Di Carlo, *IEEE Trans. Nanotechnol.* **2016**, *15*, 255.
- [49] P. A. Shaikh, D. Shi, J. R. D. Retamal, A. D. Sheikh, M. A. Haque, C. F. Kang, T. Wu, *J. Mater. Chem. C* **2016**, *4*, 8304.
- [50] W. G. Li, X. D. Wang, J. F. Liao, Z. F. Wei, Y. F. Xu, H. Y. Chen, D. B. Kuang, *J. Mater. Chem. C* **2019**, *7*, 5670.
- [51] L. H. Zeng, D. Wu, S. H. Lin, C. Xie, H. Y. Yuan, W. Lu, Y. H. Tsang, *Adv. Funct. Mater.* **2019**, *29*, 1806878.
- [52] M. Zhang, F. Zhang, Y. Wang, L. J. Zhu, Y. F. Hu, Y. B. Hou, Z. D. Lou, F. Teng, *Sci. Rep.* **2018**, *8*, 11157.
- [53] L. Lv, F. W. Zhuge, F. J. Xie, X. J. Xiong, Q. F. Zhang, N. Zhang, Y. Huang, T. Y. Zhai, *Nat. Commun.* **2019**, *10*, 3331.
- [54] Z. X. Zhang, C. Li, Y. Lu, X. W. Tong, F. X. Liang, X. Y. Zhao, D. Wu, C. Xie, L. B. Luo, *J. Phys. Chem. Lett.* **2019**, *10*, 5343.